RESEARCH ARTICLE

WILEY

Both noise-floor and tissue compartment difference in diffusivity contribute to FA dependence on *b*-value in diffusion MRI

Junye Yao [1,2] | Benjamin C. Tendler [3] | Zihan Zhou [1,2] | Hao Lei [4] | Lei Zhang [5,6] | Aimin Bao [5,6] | Jianhui Zhong [1,2,7] | Karla L. Miller [3] | Hongjian He [1,2]

[1]Center for Brain Imaging Science and Technology, College of Biomedical Engineering and Instrument Science, Zhejiang University, Hangzhou, Zhejiang, China

[2]Key Laboratory for Biomedical Engineering of Ministry of Education, Zhejiang University, Hangzhou, Zhejiang, China

[3]Wellcome Centre for Integrative Neuroimaging, FMRIB, Nuffield Department of Clinical Neurosciences, University of Oxford, Oxford, UK

[4]State Key Laboratory of Magnetic Resonance and Atomic and Molecular Physics, Innovation Academy for Precision Measurement Science and Technology, Chinese Academy of Sciences, Wuhan, China

[5]Department of Neurology in Second Affiliated Hospital, Key Laboratory of Medical Neurobiology of Zhejiang Province, and Department of Neurobiology, Zhejiang University, Hangzhou, China

[6]National Human Brain Bank for Health and Disease, School of Brain Science and Brain Medicine, Zhejiang University, Hangzhou, China

[7]Department of Imaging Sciences, University of Rochester, Rochester, New York, USA

Correspondence
Hongjian He, Zhejiang University, Zhouyiqing Building, Room 314, Yuquan Campus, Hangzhou 310027, China.
Email: hhezju@zju.edu.cn

Abstract

Noninvasive diffusion magnetic resonance imaging (dMRI) has been widely employed in both clinical and research settings to investigate brain tissue microstructure. Despite the evidence that dMRI-derived fractional anisotropy (FA) correlates with white matter properties, the metric is not specific. Recent studies have reported that FA is dependent on the *b*-value, and its origin has primarily been attributed to either the influence of microstructure or the noise-floor effect. A systematic investigation into the inter-relationship of these two effects is however still lacking. This study aims to quantify contributions of the reported differences in intra- and extra-neurite diffusivity to the observed changes in FA, in addition to the noise in measurements. We used in-vivo and post-mortem human brain imaging, as well as numerical simulations and histological validation, for this purpose. Our investigations reveal that the percentage difference of FA between *b*-values (pdFA) has significant positive associations with neurite density index (NDI), which is derived from in-vivo neurite orientation dispersion and density imaging (NODDI), or Bielschowsky's silver impregnation (BIEL) staining sections of fixed post-mortem human brain samples. Furthermore, such an association is found to be varied with Signal-to-Noise Ratio (SNR) level, indicating a nonlinear interaction effect between tissue microstructure and noise. Finally, a multicompartment model simulation revealed that these findings can be driven by

differing diffusivities of intra- and extra-neurite compartments in tissue, with the noise-floor further amplifying the effect. In conclusion, both the differences in intra- and extra-neurite diffusivity and noise-floor effects significantly contribute to the FA difference associated with the *b*-value.

1 | INTRODUCTION

By detecting water random motion processes, diffusion magnetic resonance imaging (dMRI) can noninvasively characterize tissue microstructures in the living brain (Basser, 1995; Pierpaoli & Basser, 1996). Diffusion tensor imaging (DTI) is one of the most common models in dMRI used to characterize the anisotropy of water diffusion in tissue for more than two decades. Towards better characterization of neural tissues, several advanced models such as diffusion kurtosis imaging (DKI) (Jensen et al., 2005; Lu et al., 2006) and neurite orientation dispersion and density imaging (NODDI) (Zhang et al., 2012), have also been proposed, allowing estimation of higher-order parameters and more accurately describe the water diffusion in complex tissue structures by accounting for non-Gaussian diffusion. Despite the emergence of these more advanced dMRI models, DTI continues to play an important role in studying the WM associated with both normal physiological and pathophysiological alterations in both research and clinical studies, including brain development and aging (Mårtensson et al., 2018; Qiu et al., 2015), neurodegenerative diseases (Bledsoe et al., 2018; Kantarci et al., 2017), psychiatric disorders (Olvet et al., 2014; Repple et al., 2017), brain injuries, and tumor (Asken et al., 2018; Maj et al., 2020).

Two fundamental influencing factors in DTI are diffusion weighting and signal-to-noise ratio (SNR). Other considerations include spatial and angular resolution, diffusion time, echo time, and so forth. In conventional Pulsed-Gradient Spin-Echo (PGSE) sequences (Stejskal & Tanner, 1965), the *b*-value, a factor that reflects the gradient strength and duration used to determine the degree of diffusion weighting and thus the sensitivity of the measurement to diffusive motion, is determined by the gradient strength (*G*), gradient duration (*δ*), and spacing of these pulsed gradients defined by the diffusion time (Δ). As the *b*-value increases, the measured diffusion signal decays more, resulting in a lower signal-to-noise ratio (SNR). In addition, noise in dMRI also varies with imaging resolution, field strength, echo time, etc. In particular, Rician-distributed noise in the image domain would introduce significant bias into the model estimation. While the two factors of *b*-value and noise have been discussed separately in the previous literature, to the best of our knowledge, their interaction has not been thoroughly investigated or fully understood. A comprehensive study on this topic would help to improve our current knowledge of the dMRI signal mechanism and the relationship between model parameters and underlying microstructure.

In DTI, the effect of the *b*-value on the scalar metric of fractional anisotropy (FA) has previously been studied. While some studies reported nonsignificant differences (Bisdas et al., 2008; Melhem et al., 2000), other studies supported that higher *b*-values, at a given diffusion time, are linked to a lower FA (Barrio-Arranz et al., 2015; Farrell et al., 2007; Jones & Basser, 2004; Landman et al., 2007; Lerma-Usabiaga et al., 2019; Metzler-Baddeley et al., 2012; Mukherjee et al., 2008; Veraart et al., 2011; Wu et al., 2013). This observation has previously been attributed to noise-floor bias (Barrio-Arranz et al., 2015; Farrell et al., 2007; Jones & Basser, 2004; Landman et al., 2007; Mukherjee et al., 2008). This noise impact was considered to be substantially reduced when the SNR in raw DWIs is higher than 20 (Bastin et al., 1998; Hui et al., 2010). The models for measuring non-Gaussian diffusion would improve the characterization of tissue microstructure by minimizing confounding from noise floor effects (Guo et al., 2019; Hui et al., 2008; Raab et al., 2010). The DTI model assumes that water displacements correspond to a Gaussian distribution, which is not true when water is restricted or exists in multiple compartments with different diffusivities (Mori & Zhang, 2006). Thus, the FA derived from the diffusion kurtosis imaging (DKI) model was found less dependent on the *b*-value after the kurtosis terms were added (Veraart et al., 2011) to account for the complex anisotropic microstructures (Wu et al., 2013). In other studies, the diffusion signal has been modeled as the combination of the signals coming from the restricted intracellular space (slow pool) and the tortuous and hindered extracellular space (fast pool) (Bihan, 2007; Clark et al., 2002; Clark & Bihan, 2000; Niendorf et al., 1996). The fast pool water signal decays faster as the *b*-value increases, making the measurement dependent on *b*-values. However, assuming that extracellular water is more rapidly diffusing will lead to higher FA at high *b*-values (Clark et al., 2002), which is in contrast to recent findings that higher *b*-values are linked to a lower FA. As the above brief literature review demonstrated, the FA dependence on the *b*-value has been attributed to multiple sources, including rectified noise-floor effects (Farrell et al., 2007; Jones & Basser, 2004; Landman et al., 2007) or the inaccuracies of the Gaussian model (Veraart et al., 2011; Wu et al., 2013), all of which likely are contributing to different degrees in any given experiment depending on the details of the acquired data.

The objective of this study is to explore the interplay of the aforementioned noise-floor effects and tissue microstructure on the dependence of FA on *b*-values. To achieve this aim, we built a multi-compartment framework based on different diffusivities between the

intra- and extra-neurite compartments. We hypothesize that both the relative compartmental fractions and noise levels would have impact on the fitted tensor and its derived scalar metrics, such as apparent diffusion coefficient (ADC) and FA. We used in-vivo and post-mortem human brain imaging, in addition to mathematical simulations and histological validation. The percentage difference of FA (pdFA, defined in Equation (1)) was found to be positively correlated with intra-neurite volume fraction (INVF) in the simulations. As expected, similar significant associations were identified between pdFA and NDI in both in-vivo and post-mortem experiments. The numerical simulations confirm how diffusivity profiles, intra-neurite fractions, and noise-floor contributions affect the FA dependence on b-value. Furthermore, the association between pdFA and NDI varied with SNR level, as demonstrated by both in-vivo and simulation results, indicating a nonlinear interaction effect between tissue microstructure and noise. These findings suggest that both tissue compartment diffusivity differences and the noise-floor effects contribute to the observed FA dependence on b-value in diffusion MRI.

2 | MATERIALS AND METHODS

2.1 | Data sets

2.1.1 | In-vivo experiment

In this investigation, two in-vivo data sets, each containing 61 individuals, were analyzed. One from our recruited healthy volunteers (mean age: 35.9 ± 14.1 years, range: 20–69 years, 24 males) and the other from the Human Connectome Project (HCP) (Van Essen et al., 2013). The study was approved by the local ethical committee.

In the first data set, all participants were given written informed consent and then underwent an MRI scan on a 3T MAGNETOM Prisma scanner (Siemens Healthcare, Erlangen, Germany) equipped with a 64-channel head–neck coil. Anatomical T1-weighted images were acquired using a 3D magnetization-prepared two rapid acquisition gradient echo (MP2RAGE) sequence (TR/TE = 5000/2.9 ms, TI = 700, 2500 ms, FOV = $211 \times 256 \times 256$ mm^3, voxel size = $1.2 \times 1 \times 1$ mm^3, bandwidth = 240 Hz/Px, iPAT factor = 3, and TA = 8 min) (Marques et al., 2010). Diffusion-weighted (DW) images were obtained using a simultaneous multislice (SMS) diffusion EPI prototype sequence (TR/TE = 5400/71 ms, diffusion time (Δ) = 34.4 ms, gradient time (δ) = 15.9 ms, FOV = 220×220 mm^2, slice number = 93, voxel size = $1.5 \times 1.5 \times 1.5$ mm^3, bandwidth = 1712 Hz/Px, iPAT factor = 2, and SMS factor = 3) (Setsompop et al., 2012), with anterior to posterior (AP) and posterior to anterior (PA) phase encoding directions, number of averages (NA) = 2. The diffusion scheme, containing 30 gradient directions with uniform angular coverage on each shell (b-value = 1000, 2000, and 3000 s/mm^2, noncollinear among all shells) and six nondiffusion volumes equally separated in the scheme for the motion estimation. The total acquisition time for DW images was 19 min.

The second data set was selected randomly from the Human Connectome Project (HCP) (Van Essen et al., 2013) with matched number of subjects and analyzed using the same pipeline. In this data set, nominal resolution was 1.25 mm isotropic, with 90 noncollinear gradient directions on each shell (b-value = 1000, 2000, and 3000 s/mm^2) TR/TE = 5900/89 ms, diffusion time (Δ) = 43 ms, gradient time (δ) = 10.6 ms, iPAT factor = 1, and SMS factor = 3. We down sampled the Dir90 to Dir30, chosen to maximize the angular distance between encoding vectors in order to ensure sufficient angular coverage for each under-sampling scheme (Aliotta et al., 2019). The results of DTI fitting with 90 directions and 30 directions were compared to study the impact of precision on the quantification of FA. The results of HCP data sets are reported in Table S7, Table S8 and Figure S4.

2.1.2 | Post-mortem experiment

A left hemisphere sample of a donated post-mortem human brain sample (76-year-old, male, 525 min post-mortem interval) was obtained from the National Human Brain Bank for Health and Disease, China. Prior to death, the donor had been registered at the Zhejiang University School of Medicine and signed informed authorization for the use of his tissue and medical records for research purposes. This study was conducted with the prior approval of the ethics committee of Zhejiang University School of Medicine.

For the first 4 weeks, the hemisphere was immersed in 10% formalin. It was then rinsed with tap water for 24 h to partially restore the relaxation parameters (Jonkman et al., 2019; Shepherd et al., 2009). The sample was placed in a container full of Fomblin (Fomblin, YL VAC25/6, Solvay) after wiping the water off the surface. Prior to the MR scan, air bubbles were extracted from the containers using a vacuum pump, and the sample was kept at room temperature (22 $\pm$ 0.5°C) for 24 h.

MR scans were conducted with the same MAGNETOM Prisma 3T scanner and the 64-channel coil. DW images were obtained with a Readout-Segmented Echo-Planar Imaging (RS-EPI) sequence (Porter & Heidemann, 2009). DWI was performed with five b-values (1000, 2000, 4000, 6000, and 8000 s/mm^2) over 30 gradient directions on each b value, with one nondiffusion weighted data set acquired after every 10 DW images. Other parameters included: TR = 9620 ms, TE = 96 ms/118 ms, δ = 35.7 ms, Δ = 46.3 ms, FOV = 198×198 mm^2, readout segments = 5, number of averages (NA) = 2, voxel size = $1.8 \times 1.8 \times 1.8$ mm^3 and bandwidth = 1190 Hz/pixel. The scan took 4 h and 24 min in total.

2.2 | Image processing

Both the in-vivo and post-mortem diffusion images were preprocessed using FSL (FMRIB software library, University of Oxford, UK), which was used to perform field map estimation, eddy current-induced distortion correction, and head motion correction. A linear

transformation was applied to the T1-weighted image for each subject to align with the DW images.

For each participant, we have the NA = 1 (containing only AP phase encoding data sets) and NA = 2 data sets. The latter offers a higher level of SNR and increases the measurement precision. The DTI estimates (FA) were calculated per shell of in-vivo DW images with weighted linear squares (WLS) fitting using FSL "dtifit" function.

The noise in the complex MR signal is normally distributed, whereas the magnitude signal used in dMRI is approximately Rice distributed (Gudbjartsson & Patz, 1995). As increasing average times will not reduce the Rician bias, FA was also estimated using maximum likelihood estimators (MLE) (https://github.com/imphys/fit-diffusion-model.git) to account for the Rician bias in the magnitude dMRI signal, and then compared with traditional WLS fitting.

DW data from all three shells were additionally fitted to the NODDI model using the NODDI toolbox (https://www.nitrc.org/projects/noddi_toolbox) to obtain neurite density index (NDI-NODDI). To further verify the influence of non-Gaussian diffusion, mean kurtosis (MK) was computed from three-shell data using the open-source software DESIGNER (https://github.com/NYU-DiffusionMRI/DESIGNER/), with constraints of D_{app} >0 and K_{app} >0 employed.

For post-mortem DW data, the first two b-shells of 1000 and 2000 s/mm^2 were discarded from the further investigation due to the reduced diffusivity of the fixed corpus callosum. ADC measured with dMRI has been reported to be reduced by as much as 50% in unfixed post-mortem WM and 80% in fixed WM with respect to in-vivo values (D'Arceuil et al., 2007), which strongly reduces the contrast-to-noise ratio in dMRI (D'Arceuil et al., 2007; Shepherd et al., 2009). Because the signal distribution deviated from the Rician distribution more, we only used WLS with "dtifit" to fit the ex-vivo data. The remaining images were preprocessed similarly to the in-vivo data. Tensor model fitting was performed individually on b-shells of 4000, 6000, and 8000 s/mm^2, respectively. Only FA differences between b-values of 4000 and 8000 s/mm were considered in further analysis to allow for enough diffusion weighting difference. The low SNR condition (NA = 1) was not analyzed in modeling fitting due to insufficient SNR at a b-value of 8000 s/mm^2.

2.3 | ROI definition

2.3.1 | In-vivo data

The JHU DTI-based white-matter atlases (Mori et al., 2005) were used to create regions of interest (ROIs), including six white matter tracts (anterior limb of the internal capsule, posterior limb of the internal capsule, superior longitudinal fasciculus, genu of the corpus callosum, body of the corpus callosum, and splenium of the corpus callosum). To see how it performs in regions other than parallel fibers, cortical gray matter regions from an HCPMMP1 (Glasser et al., 2016) parcellation in the MNI space (downloaded from HCP-MMP1.0 projected on MNI2009a GM [volumetric]), subcortical gray matter regions from Harvard-Oxford Cortical Structure Atlas, and manually drawn WM regions with crossing fibers in a region of the brain containing crossing

fibers of the superior corona radiata (SCR) and the body of the corpus callosum (BCC) were also selected (Figure S4). The details of these ROIs are reported in Tables S1–S6.

Individual T1w images (aligned at DW images) were first normalized to MNI space using FSL's linear and nonlinear registration tools (FLIRT, FNIRT) for each subject to acquire the transformation matrix. The ROI masks were then inversely transformed from atlas space to native DW image space using the inverse of the derived transformation matrix. Diffusion metrics were then averaged within each ROI.

2.3.2 | Post-mortem data

The stained sections in the post-mortem experiment have a comparable thickness (6 μm) to the size of axons (∼1 to 2 μm) (Coelho et al., 2018), and may introduce bias related to axon orientation dispersion. Therefore, the lateral to the midline of the corpus callosum was chosen as ROI to minimize this bias, since it has highly parallel-aligned fiber bundles and most slices were expected to be perpendicular to the axon axis. It is worth noting that we only obtained 2D histology staining data and estimated NDI-Histology using the neurite area fraction (Schmierer et al., 2004). In order to perform correlation analysis between 3D post-mortem DW images and 2D histology stained sections, cortical anatomical landmarks (Figure 1b,c) were used to determine the slice selection of each ROI as in previous studies (Cardenas et al., 2017; Jonkman et al., 2016; Zhou et al., 2020). MRIcron (https://www.nitrc.org/projects/mricron) was used to manually draw ROIs on coronal views of DW images. To strike a compromise between the best match with histology sections and statistical robustness, the surface areas of ROIs of dMRI were kept at 48.6 mm^2 (containing 15 voxels distributed over 2 coronal slices. The surface areas of histological sections used to estimate NDI-histology are around 45 mm^2). Given the relatively small number of voxels within each ROI, the median value was calculated for the MRI metrics, and the pdFA between b-values of 4000 and 8000 s/mm^2 was subsequently calculated.

2.4 | Histological quantification of stained sections

After MRI, the hemisphere sample was sectioned in 5 mm thick coronal blocks. This process yielded six slices with their locations drawn in sagittal MR images as shown in Figure 1a.

Corpus callosum tissue blocks were processed for embedding in paraffin and cutting in sections with a thickness of 6 μm. The tissue sections were histochemically stained for neurites by use of Bielschowsky's silver impregnation (BIEL) technique (Schmierer et al., 2004) (Figure 1d). The histological specimens were matched to the initial post-mortem MRI manually. Digitization of the stained sections was performed on a Virtual Slide Microscope (VS120, OLYMPUS, Japan) using a 10× magnifying objective, which led to a resolution of 0.69 μm/pixel. The neurite density in the corpus callosum was quantified in BIEL-stained sections using Image-J (https://imagej.nih.gov/ij).

FIGURE 1 MRI, tissue blocks, and corresponding tissue stains. (a) a sagittal magnetic resonance (MR) T1-weighted image showing the marked locations of the 6 histology samples, with a single coronal slice indicated by the blue line shown in (b) coronal MR T1-w image and (c) digital photo of tissue blocks. Histological section (d) shows Bielschowsky's silver impregnation (BIEL) staining of the area corresponding to the rectangular blue blocks in (b) and (c). (e) Zoom-in part of the cracked area in (d) marked by a red rectangular, cracks and imperfections with boundaries in yellow were eliminated at this step to reduce the error of neurite density estimation. The super-threshold pixels in red indicate the neurite parts
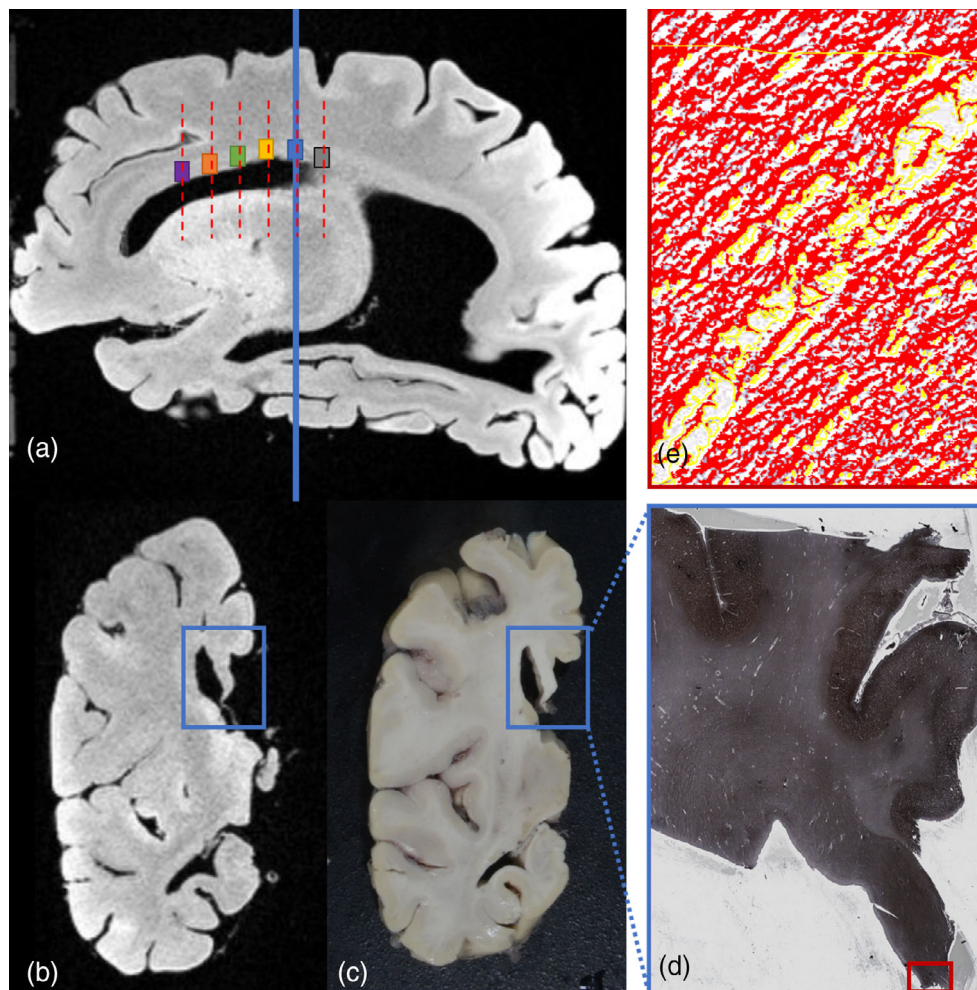
The boundaries of ROIs were manually delineated on the corpus callosum to exclude the slice's background, after which each slice was converted to 8-bit format, and a slice-wise threshold computed with the default ISODATA algorithm was set to eliminate cracks and imperfections (Figure 1e). Following that, BIEL stains were color deconvoluted (Bagnato et al., 2018; Zhou et al., 2020), yielding three channels (Figure S1). As Channel 1 was predominantly represented by neurite staining with little contribution from the background, it was used for subsequent statistics. We used ImageJ to quantify neurite density, which was expressed as a percentage of the ROI's area. Only effective stained voxels that passed a threshold determined by the maximum entropy threshold algorithm were used. Examples of these two phases are depicted in Figure S1.

2.5 | Statistical analysis

For the in-vivo data, we first performed one-sided paired t-tests over the whole brain (in MNI space) to examine if the FA value decreased as the b value increased. Voxel-level family-wise error (FWE)-corrected was applied with the family-wise error rate of 0.05. This was performed using SPM12 (http://www.fil.ion.ucl.ac.uk/spm/software/spm12/).

In order to investigate how FA changes with b-value quantitatively, a percentage difference of FA (pdFA) between distinct b-values was defined as follows:

$$pdFA_{ab} = \frac{FA(b_a) - FA(b_b)}{mean[FA(b_a), FA(b_b)]} \times 100\%, \ (b_a < b_b) \qquad (1)$$

Pearson's correlation analysis was conducted among the pdFAs derived from different b-values and MK from DKI and NDI from NODDI to investigate the relationship of pdFA with other current high-order diffusion models. The resulting statistical measures were corrected for multiple tests using the False Discovery Rate (FDR [Benjamini & Hochberg, 1995]). In addition, the relationship between pdFA and NDI-Histology was also investigated with the post-mortem data. All analyses were performed using MATLAB 2019b (MathWorks, Natick, MA, USA).

2.6 | Model simulations

We are interested in the effect of compartmental water diffusivity on FA values measured at various diffusion gradient strengths. In a "standard model" (Novikov et al., 2019), it is assumed that diffusion signal

in a WM voxel comes from three nonexchanging sources: the intra- and extra-axonal space of neurites, and a free water compartment. Each compartment has a distinct diffusion profile (denoted as D_{in}, D_{en}, D_{iso}, respectively). As a result, the overall signal for a typical WM configuration under this model can be simulated as follows (Harms et al., 2017):

$$S = f_{in} \cdot S_0 e^{-bD_{in}} + f_{en} \cdot S_0 e^{-bD_{en}} + f_{iso} \cdot S_0 e^{-bD_{iso}} \tag{2}$$

$$f_{in} + f_{en} + f_{iso} = 1 \tag{3}$$

$$\text{INVF} = \frac{f_{in}}{f_{in} + f_{en}} \tag{4}$$

where f denotes the signal fraction of the intra-neurite (f_{in}), extra-neurite (f_{en}), and free water (f_{iso}) compartments respectively, and intra-neurite volume fraction (INVF) is represented by Equation (4). The intra-neurite space is modeled as a collection of infinitely long cylinders (radial diffusivity, $D_{in}^{\perp} = 0$), and the extra-axonal space is assumed to behave as a Gaussian anisotropic medium. Recent works suggested that under in-vivo conditions, $D_{in}^{\parallel} > D_{en}^{\parallel}$ (Dhital et al., 2018; Jespersen et al., 2018; Kunz et al., 2018), with $D_{in}^{\parallel} \approx 2.2 - 2.5 \times 10^{-3} \text{ mm}^2/\text{s}$ (Dhital et al., 2019; Mckinnon et al., 2018). In this work, we assumed that $D_{in}^{\parallel} = 2.5 \times 10^{-3} \text{ mm}^2/\text{s}$, $D_{en}^{\parallel} = 0.78 \times 10^{-3} \text{ mm}^2/\text{s}$, and $D_{en}^{\perp} = 0.65 \times 10^{-3} \text{ mm}^2/\text{s}$ for WM (Kunz et al., 2018), and $D_{iso} = 3 \times 10^{-3} \text{ mm}^2/\text{s}$ in vivo (Alexander et al., 2010; Zhang et al., 2011). For simplicity, the three components are assumed to be perpendicular to the main magnetic field, and sub-bundles were not considered. The diffusion gradient tables of the simulated data were identical to the in-vivo data protocol. In order to capture more subtle changes in FA, we added additional data sets with b-values of 700, 1500, and 2500 s/mm² besides the existing 1000, 2000, and 3000 s/mm² of the experimental data.

All the simulated diffusion signals at different b-values and SNR levels were fitted with a diffusion tensor model to estimate the diffusion parameters.

Three sets of simulation experiments were carried out in all. In *Simulation I*, we considered a pure white matter structure with two-compartment (e.g., without free water) and single compartment constitutions, to verify whether the reported compartmental difference of diffusivity could lead to the underestimation of FA. The relationship between FA and b-value was investigated at various noise levels to investigate the effect of the rectified noise-floor on the estimated FA. Then in *Simulation II*, we looked at a more general case with a partial fraction of free water (e.g., three compartments), and the influences of high and anisotropic diffusivity of free water compartment on estimated FA were investigated. Furthermore, *Simulation III* was run to look into the inter-relationship between noise-floor effects and the microstructure contribution of the intra-neurite fraction to the FA difference, and the shapes of the ADC profile were also estimated.

2.6.1 | Simulation I

Firstly, we considered a voxel of pure white matter, with only intra- and extra-axonal neurite spaces, defining $f_{in} = 0.6$ (Chang et al., 2015), $f_{en} = 0.4$, and $f_{iso} = 0$. The magnitude MR signal was simulated for 1000 random Rician noise realizations, with SNR levels ranging from 20, 30, 60, and noise-free. The noise levels were chosen to approximate the low, median, and upper bands of the in-vivo human dMRI data set (NA = 2). Rician noise was added to the signal S in the following fashion (Tuch, 2004):

$$S_{\text{noisy}} = \sqrt{(S + \epsilon 1)^2 + \epsilon 2^2} \tag{5}$$

where $\epsilon 1, \epsilon 2 \sim N(0, \sigma^2)$, $\sigma = S_0/\text{SNR}$ corresponds to a given signal-to-noise ratio (SNR). The signal was simulated for 1000 random Rician noise realizations to achieve convergence (for every SNR condition, we assume $S_0 = 1$ without loss of generality, keep σ fixed, $\epsilon 1$ and $\epsilon 2$ are randomly generated).

A further single-compartment model was also run with the same apparent diffusivity coefficient (AD = 1.81×10^{-3} mm²/s, RD = 0.27×10^{-3} mm²/s), to compare the above two-compartment configuration. Diffusivity coefficients of intra-(AD = 2.5×10^{-3} mm²/s, RD = 0×10^{-3} mm²/s) and extra-neurite (AD = 0.78×10^{-3} mm²/s, RD = 0.65×10^{-3} mm²/s) compartments were also performed to explore the effects of noise on different compartments. All other parameters were kept the same.

2.6.2 | Simulation II

In general, free water is isotropic and has the highest diffusivity value. The fully isotropic free water compartment contributes less to the diffusion signal at a higher b-value, causing FA to deviate from isotropy, according to the hypothesis.

We simulated a voxel of WM affected by free water at SNR = 30 and in the absence of noise, which can be achieved by set $f_{iso} = 0.1$, $INVF = 0.6$ ($f_{in} = 0.54, f_{en} = 0.36$). The free water contribution is modeled as a Gaussian isotropic compartment with fixed free diffusivity $D_{iso} = 3 \times 10^{-3}$ m²/s in vivo (Alexander et al., 2010; Zhang et al., 2011). All other options were the same as *Simulation I*.

2.6.3 | Simulation III

To further explore how intra-neurite volume fraction and noise-floor effects jointly contribute to FA change with different b-values, a total number of 61 INVFs were randomly generated, ranging from 0.5 to 0.8 as measured in WM of our in-vivo data. The simulations were then performed at each INVF with SNR ranging from 15 to 100, and noise-free cases. Other options were the same as *Simulation I*.

3 | RESULTS

3.1 | In-vivo experiments

3.1.1 | FA dependence on *b*-value

In-vivo human brain experiments demonstrate that as the *b*-value increased, FA decreased (Figure 2). Based on one-sided paired t-tests at the group level, the drop in white matter FA was statistically significant ($p < .05$). The FA profiles of representative white matter ROIs are shown in Figure 3a. FA values of all ROIs were consistently maximal at b1000 and gradually declined at b2000 and b3000. This finding was further supported by the post-mortem experiment, which showed that FA values of b4000 are consistently larger than those of b8000 in slices of corpus callosum (Figure 3b).

3.1.2 | Relationship between pdFA and MK & NDI-NODDI for in-vivo data

The relationships of pdFA with high-order diffusion models were investigated. At the high SNR condition (NA = 2) of the in-vivo experiment, the $pdFA_{13}$ estimated by WLS was shown to be significantly and positively correlated with both MK (Figure 4) and NDI-NODDI (Figure 5). Significant associations were identified across all $pdFA_{13}$ estimates for MK (Table 1) and NDI-NODDI (Table 2). As for $pdFA_{12}$ and $pdFA_{23}$, GCC showed slight and nonsignificant correlations. By contrast, when the SNR becomes lower with NA = 1, the observed correlations between pdFA and MK, NDI-NODDI were systematically smaller. The WLS estimated FA is less affected by number of averages. The significant correlation between pdFA estimated by MLE and MK, NDI still remains, though the MLE estimated pdFA has an overall decrease. However, these correlations
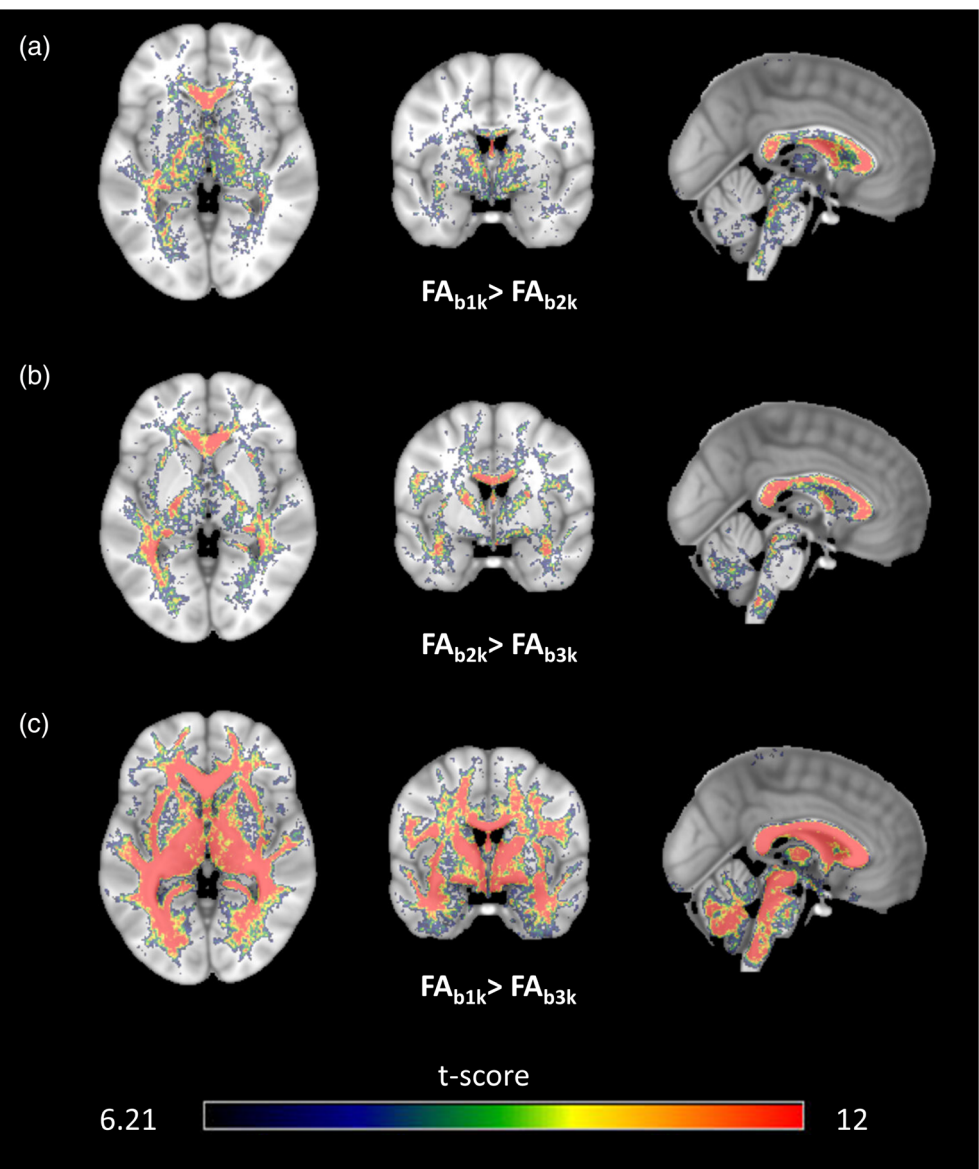

FIGURE 2 Results of group-level one-sided student's paired *t*-tests. The spatial maps were visualized at $t > 6.21$ (the threshold of significant *t*-value after FWE corrected). Positive *t*-values indicate FA(b_{low}) > FA(b_{high}). FA value decreases with increasing *b*-values, particularly noticeable across the white matter
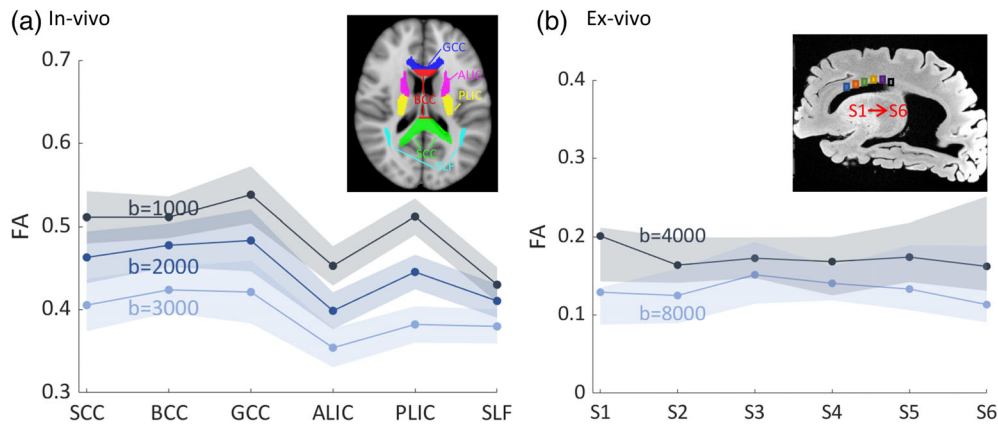
FIGURE 3 The in-vivo (a) and post-mortem (b) investigations demonstrate a relationship between FA and b-value. In each of the six representative white matter ROIs (as shown in the upper right corner in (a)), mean FA values (line) ±1SD (shaded band) of in-vivo data are shown in (a). The FA profile has a clear declining trend as the b-values increase. Similar results are shown in post-mortem data, with the median FA (line) and 25%, 75% percentile values (shaded band) of each slice (the upper right corner in (b)) shown in (b). ALIC, anterior limb of internal capsule (violet); BCC, body of corpus callosum (red); GCC, genu of corpus callosum (blue); PLIC, posterior limb of internal capsule (yellow); SCC, splenium of corpus callosum (green); SLF, superior longitudinal fasciculus (cyan)
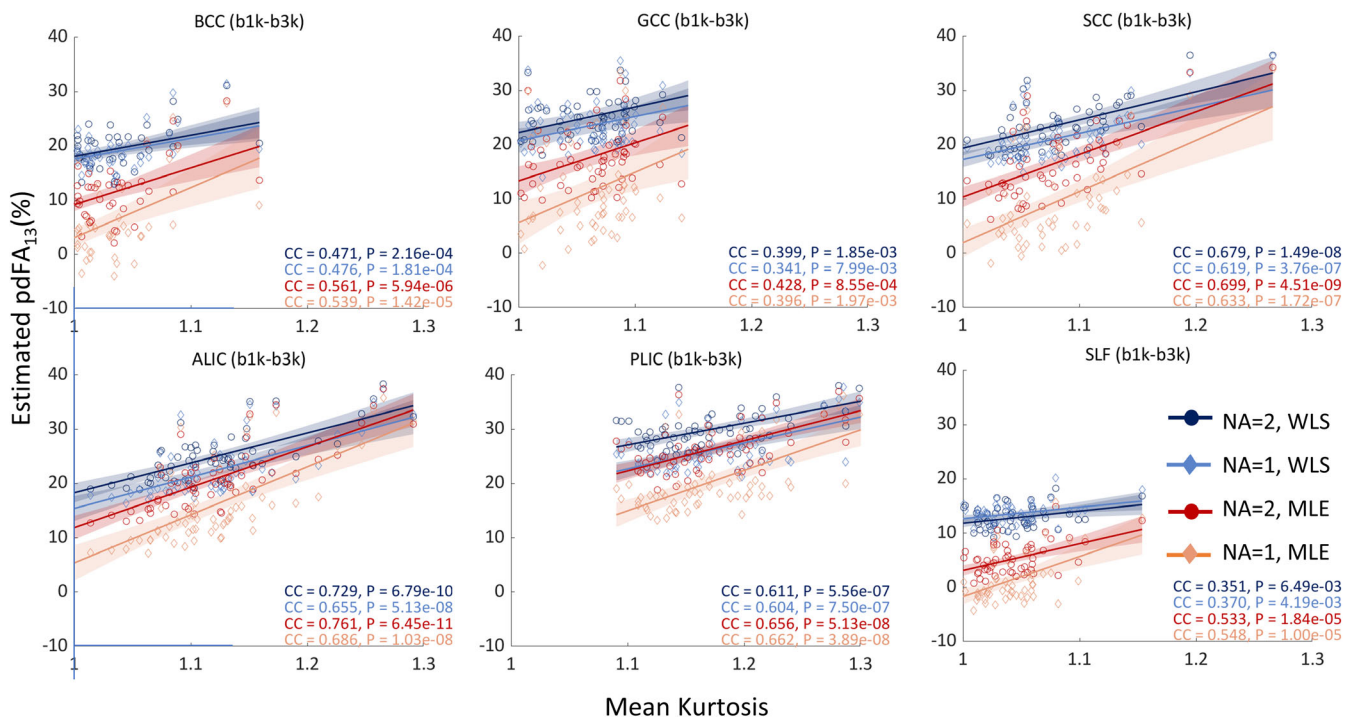

FIGURE 4 Scatter plots of pdFA$_{13}$ and MK for in-vivo data, estimated with data of different number of averages by WLS (cool color) and MLE (hot color), respectively. The best linear fits of the scatters are shown in solid lines, whereas the shaded colored areas show a 95% confidence interval. Pearson correlation coefficients and significance values are also displayed in the plots

are less significant for MLE estimated results with NA = 1. More details of the correlation coefficient (c.c.) and statistical significance values are shown in Tables 1 and 2 and Tables S1–S6, and the complete plots of pdFA$_{12}$ and pdFA$_{23}$ are shown in Figure S2 and Figure S3.

3.2 | Histological validation for ex-vivo data

Figure 6a shows that the region-wise pdFA$_{48}$ was highly correlated (c.c. = 0.869, p = .025) with NDI-Histology computed from BIEL staining of sections listed in Figure 6c, whose locations are shown in Figure 6b.
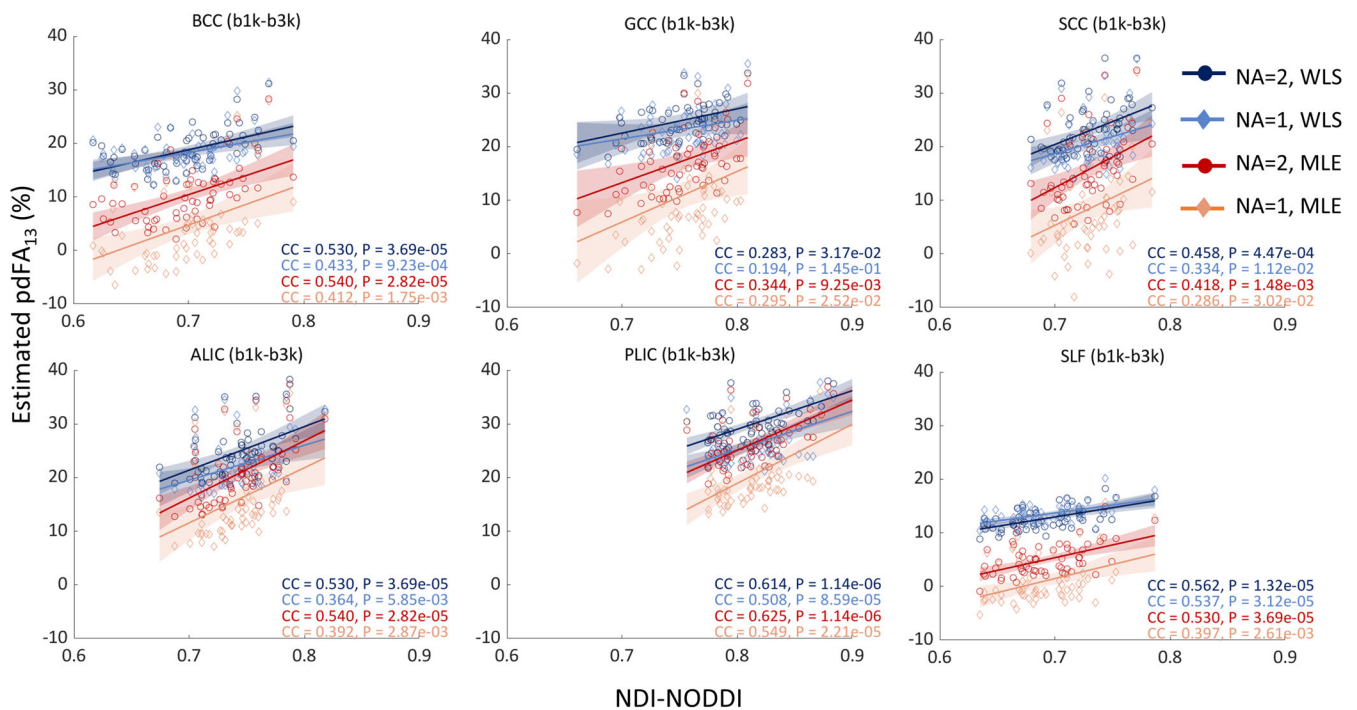
FIGURE 5 Scatter plots of pdFA$_{13}$ and NDI-NODDI for in-vivo data, estimated with data of different number of averages by WLS (cool color) and MLE (hot color), respectively. The best linear fits of the scatters are shown in solid lines, whereas the shaded colored areas show a 95% confidence interval. Pearson correlation coefficients and significance values are also displayed in the plots

TABLE 1 Statistical significance of the correlation between pdFA$_{13}$ estimated by different methods with data of different number of averages and MK

ROI	WLS			MLE		
	c.c.	Adjusted p		c.c.	Adjusted p	
SCC	0.679	1.49E−08	***	0.699	4.51E−09	***
	0.619	3.76E−07	***	0.633	1.72E−07	***
BCC	0.471	2.16E−04	***	0.561	5.94E−06	***
	0.476	1.81E−04	***	0.539	1.42E−05	***
GCC	0.399	0.002	**	0.428	8.55E−04	***
	0.341	0.008	**	0.396	0.002	**
PLIC	0.611	5.56E−07	***	0.656	5.13E−08	***
	0.604	7.50E−07	***	0.662	3.89E−08	***
ALIC	0.729	6.79E−10	***	0.761	6.45E−11	***
	0.655	5.13E−08	***	0.686	1.03E−08	***
SLF	0.351	0.006	**	0.533	1.84E−05	***
	0.370	0.004	**	0.548	1.00E−05	***

Note: * adjusted $p < .05$, ** adjusted $p < .01$, *** adjusted $p < .001$, with blue shaded cells representing NA = 2, and unshaded cell NA = 1.

TABLE 2 Statistical significance of the correlation between pdFA$_{13}$ estimated by different methods with data of different number of averages and NDI-NODDI

ROI	WLS			MLE		
	c.c.	Adjusted p		c.c.	Adjusted p	
SCC	0.458	4.47E−04	***	0.418	0.001	**
	0.334	0.011	*	0.286	0.030	*
BCC	0.530	3.69E−05	***	0.540	2.82E−05	***
	0.433	9.23E−04	***	0.412	0.002	**
GCC	0.283	0.032	*	0.344	0.009	**
	0.194	0.145		0.295	0.025	*
PLIC	0.614	1.14E−06	***	0.625	1.14E−06	***
	0.508	8.59E−05	***	0.549	2.21E−05	***
ALIC	0.530	3.69E−05	***	0.540	2.82E−05	***
	0.364	0.006	**	0.392	0.003	**
SLF	0.562	1.32E−05	***	0.530	3.69E−05	***
	0.537	3.12E−05	***	0.397	0.003	**

Note: * adjusted $p < .05$, ** adjusted $p < .01$, *** adjusted $p < .001$, with blue shaded cells representing NA = 2, and unshaded cell NA = 1.

3.3 | Model simulations

3.3.1 | Simulation I

In *Simulation I* with $INVF = 0.6$ ($f_{in} = 0.6$, $f_{en} = 0.4$), and $f_{iso} = 0$, a decrease in FA with increasing b-value was observed under the noise-

free conditions of the multicompartment model (Figure 7a). It indicates that the inherent multicompartment structure could still lead to FA underestimation without Rician bias or Gaussian noise. The estimated FAs were found systemically under-estimated in all b-values, ranging from 0.81 at b1000 to 0.77 at b3000 under the noise-free condition as shown in Figure 7a. Furthermore, noise-floor will
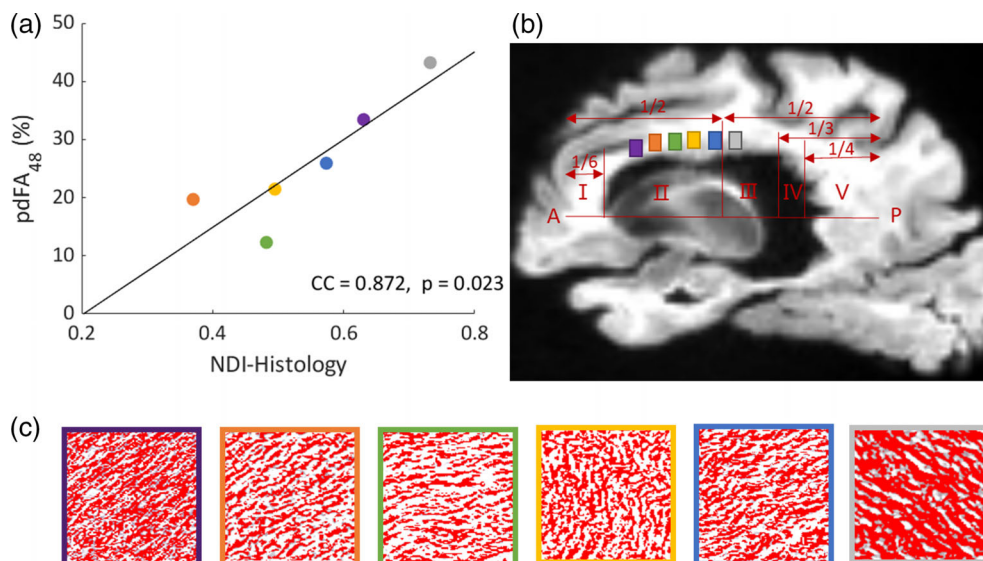
FIGURE 6 Histological analysis results for ex-vivo data. (a) Correlation between pdFA (median values in MRI ROIs) and NDI-histology of the sections. (b) Locations of MRI ROIs overlaid on a sagittal dMRI image, five vertical callosal segments based on (Hofer & Frahm, 2006) are shown in (c). (c) Topography of channel 1 output after performing color deconvolution on BIEL staining sections. Maximum entropy thresholding was applied on channel 1 to extract neurite fraction, red areas indicate the selected neurite part (pixels that exceed the threshold), which were used to estimate neurite density. The border color of the local image of the stained section in (c) matches the ROI location in (b) and the points in (a)

exacerbate the result obtained in the noise-free condition. In contrast to the other SNR levels, the estimated FA drops more dramatically at low SNR = 20. It is worth noting that when SNR > 30, the FA trend in the multicompartment model would coincide well with a noise-free case (Figure 7a).

In the single-compartment simulation, a similar tendency was discovered. The observed anisotropy is underestimated in the case of low SNR conditions and gets much worse at higher b values (Figure 7b). Most importantly, the estimated FA in the single-compartment model remained constant regardless of b-values in the absence of noise, which is remarkably different from the multicompartment simulation (Figure 7a).

The effect of noise varies in different compartments (diffusion profiles). In the intra-neurite compartment, the estimated FA decrease with b-value in the presence of noise (Figure 7c), and the lower the SNR, the more the decrease. In contrast, lower SNR leads to an overestimate in the extra-neurite compartment (Figure 7d), and FA is insensitive to changes in b values.

3.3.2 | Simulation II

When considering a WM voxel incorporating a free water compartment as shown in Figure 8, the additional fraction of free water made the results seen less intuitive in *Simulation II*. A free water compartment would weaken the reduction effect of FA under the same conditions, even cause overestimation of FA values.

When increasing the noise-floor effect (SNR = 30), the FA trend became more complicated with a small increment before b1500 and afterward gradually decreases (Figure 8a), and FA was also overestimated.

3.3.3 | Simulation III

In *Simulation III*, the interaction of noise-floor effects and intra-neurite volume fraction on pdFA was investigated (Figure 9). When INVF was varied from 0.5 to 0.8, as existed in pure white matter tissue (Chang et al., 2015), $pdFA_{13}$ was found to be significantly correlated with INVF under various SNRs. The positive correlations between pdFA and *INVF* are consistent with the experimental data (Figure 5). It is noteworthy that whereas $pdFA_{13}$ is usually larger at lower SNR conditions (Figure 9a), the correlation between $pdFA_{13}$ and INVF is greatest when the SNR is between 25 and 50, with a lesser correlation at lower or higher SNR conditions (Figure 9b).

To further illustrate these findings, changes in diffusion profiles were presented with intra-neurite volume fractions ranging from 0.5 to 0.7 in the absence of noise in Figure 10. The simulated tensors (red lines in Figure 10) have spikes due to the intra-neurite compartment ($D_{in}^{\perp} = 0$). As INVF increases, the presupposed diffusivity along with the long axis increases while in the orthogonal direction it decreases. The variance of the anisotropic measured with different b-values also increased, corresponding to the positive correlation between INVF and pdFA as shown in Figure 9.

4 | DISCUSSION

In this work, we utilized MRI of in-vivo and post-mortem human brains, histological data from a post-mortem human brain sample, and model simulations to investigate the intrinsic cause of the DTI-derived FA dependence on the b-value. We observed that FA decreased when the b-value increased (Figure 3) consistent with
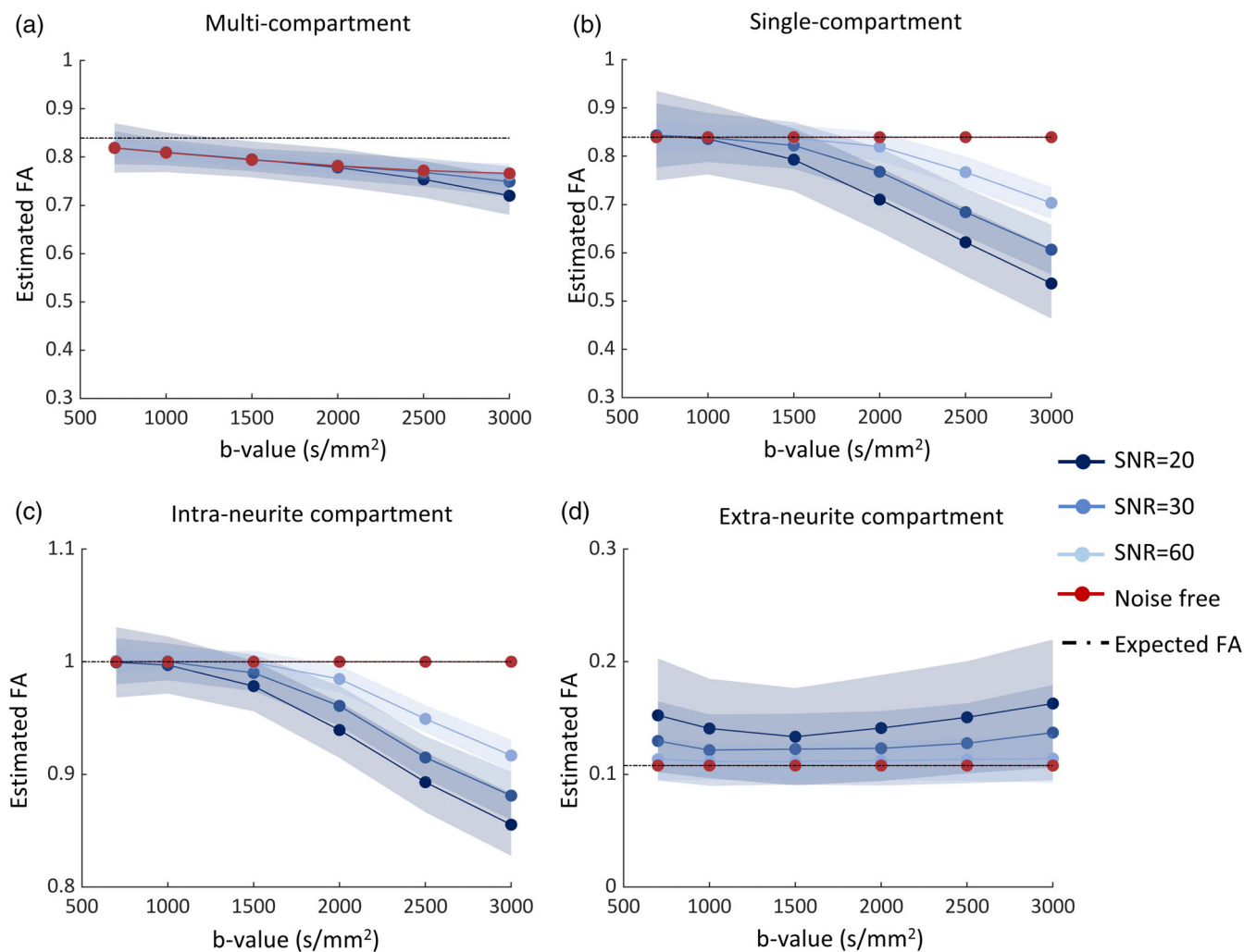
FIGURE 7 Simulation of effects of noise on FA difference for different conditions: (a) multicompartment model; (b) single-compartment model; (c) intra-neurite compartment; (d) extra-neurite compartment. Dashed lines mean the expected FA calculated based on the inherence apparent diffusivity. Different colors represent different SNR levels, shaded bands represent the range of mean ± SE. Lower SNR will cause the reduction of the estimated FA for both multi- and single-compartment models. In the case of SNR = 30 (medium blue), the simulation results are very close to the condition without noise (red) for the multicompartment model. What is more, the light line (SNR = 60) overlaps the red line (noise-free) in (a)

earlier findings (Barrio-Arranz et al., 2015; Farrell et al., 2007; Lerma-Usabiaga et al., 2019; Mukherjee et al., 2008; Veraart et al., 2011). There was a consistent relationship between the percentage difference of FA between high and low *b*-values (pdFA) and NDI-Histology generated from BIEL staining slices of fixed post-mortem human brain tissues (Figure 6a). The pdFA was similarly significantly correlated with MK and NDI-NODDI of in-vivo data (Figure 5), especially in high SNR data sets. A lower SNR would result in a higher pdFA, as well as a nonlinear effect on its correlation with NDI (Figure 9). Finally, a multicompartment model simulation revealed that the trend of pdFA against *b*-values could be due to differences in diffusion coefficient between intra- and extraneurite compartments in WM (Figure 7), with the noise-floor increasing the FA difference.

4.1 | In-vivo human brain experiments

For in-vivo experimental data, the FA profiles were similar at each *b*-value (Figure 3), which is consistent with previous findings indicating that FA values decrease as the *b*-values increase (Lerma-Usabiaga et al., 2019). Differences in FA were significant throughout white matter as shown by the results of the group-level paired *t*-test of FA values in Figure 2. As a result, we hypothesized that the drop in FA might be related to the distinctive structure of white matter. The axon, as a special structure of white matter, was considered.

We identified a strong association in the white matter between pdFA and MK (Table 1, Figure 4), a marker of microstructural complexity (Guo et al., 2019; Hui et al., 2008; Raab et al., 2010). In a previous study (Veraart et al., 2011), FA estimated from the DTI was
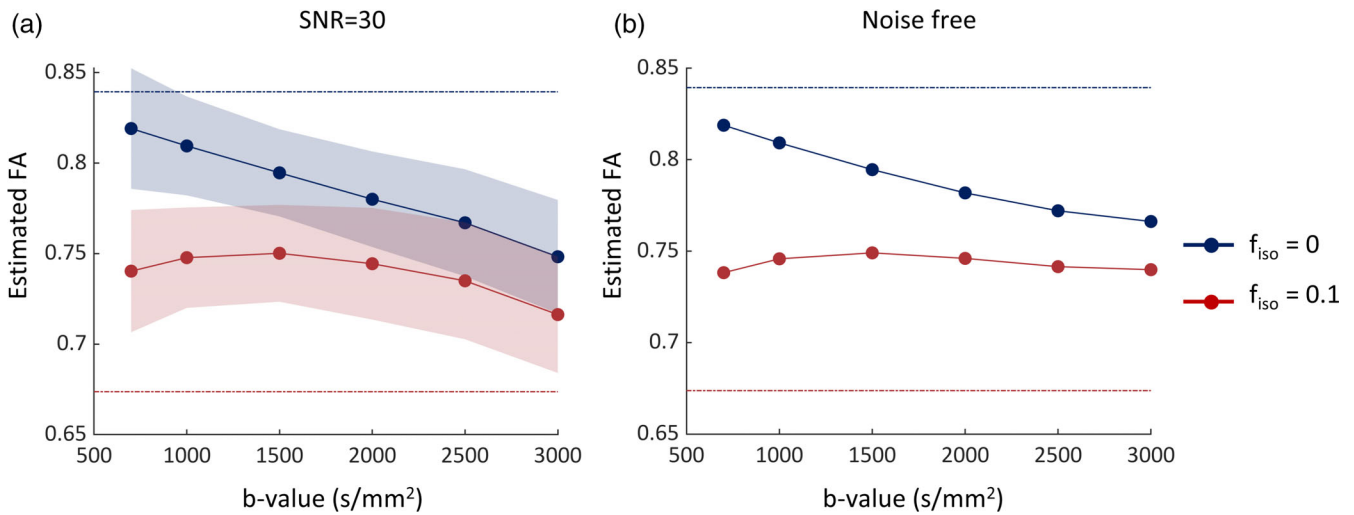
FIGURE 8 Simulation-based on the multicompartment model under different SNR. With increasing b-values, FA trend changes when other parameters are fixed: $f_{in} = 0.6$, $f_{iso} = 0$ (blue), and 0.1 (red), $D_{in}^{\parallel} = 2.5 \times 10^{-3}$ mm^2/s, $D_{in}^{\perp} = 0$, $D_{en}^{\parallel} = 0.78 \times 10^{-3}$ mm^2/s, $D_{en}^{\perp} = 0.65 \times 10^{-3}$ mm^2/s. expected FA (dashed lines of the corresponding color) for the compartmental model was calculated based on the inherence apparent diffusivity. The standard errors of noise-free conditions are smaller than $1.00 \, E{-}14$ and were not able to be shown in (b)
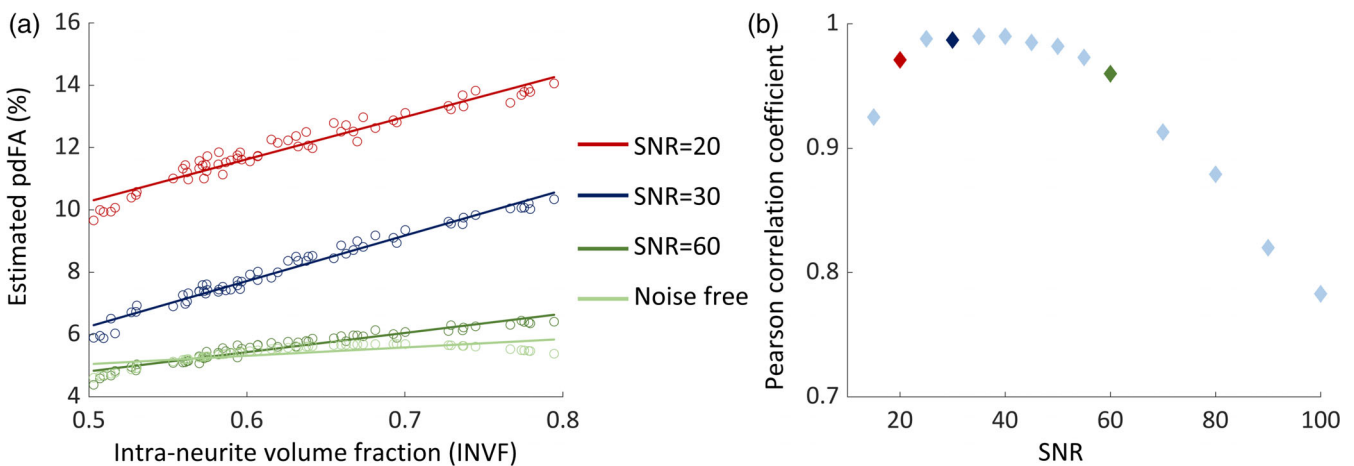

FIGURE 9 The pdFA$_{13}$ at different intra-neurite volume fractions and SNRs. The following parameters were fixed here: $f_{iso} = 0$, $D_{in}^{\parallel} = 2.5 \times 10^{-3}$ mm^2/s, $D_{in}^{\perp} = 0$, $D_{en}^{\parallel} = 0.78 \times 10^{-3}$ mm^2/s, $D_{en}^{\perp} = 0.65 \times 10^{-3}$ mm^2/s. (a) pdFA$_{13}$ change with INVF, with different colors, represent different SNRs, pdFA is globally higher at lower SNR. (b) Pearson correlation between pdFA$_{13}$ and INVF under different SNR levels, the SNR mentioned in (a) is also presented in the corresponding color in (b)

considerably reduced with a rising b-value within the range of 400–2800 s/mm^2; however, this dependency was reduced when FA was derived from DKI. The relationship between pdFA and NDI-NODDI, a metric reflecting the intra-neurite volume fraction of tissue microstructure (Fukutomi et al., 2018; Kamiya et al., 2020; Zhang et al., 2012), was also investigated. Positive correlations between pdFA$_{12}$, pdFA$_{13}$, and NDI-NODDI were found in WM areas as shown in Table 2 and Figure 5. In addition, high b-value (3000 s/mm^2) DTI redundantly parallels with NODDI-based cortical neurite measures (Fukutomi et al., 2019). Accumulating evidence has suggested that a high b-value dMRI signal is more sensitive to neurites and neural tissue changes than a low b-value dMRI signal. Compared with

traditional WLS estimated FA without considering Rician bias, the MLE estimated pdFA has an overall decrease because the maximum likelihood approach of estimating tensors from DTI data can accounts for Rician bias. As a result, the FA dependence caused by noise-floor was reduced. In this instance, microstructure was more likely to be the cause of the FA dependence on b-value. However, the performance of the current MLE algorithm may be affected by other potential causes, including the multiple-coil system (den Dekker & Sijbers, 2014).

These findings suggest that DTI metrics measured at various b-values are heterogeneous, which could be related to WM microstructure and its susceptibility to noise.

FIGURE 10 Diffusion profiles for tensor fitting with INVF ranging from 0.5 to 0.7 in the absence of noise (a–c). Three estimated diffusion profiles are shown in blue for each tensor, and the red profile corresponds to the presupposed diffusivity. The estimated diffusion tensor becomes less anisotropic with the increase of the b-value
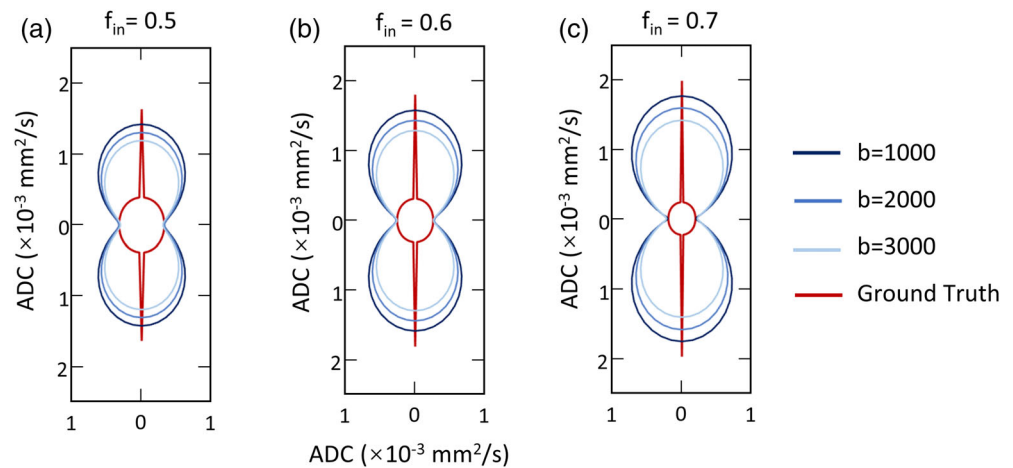
4.2 | Post-mortem human brain experiments

For histological analysis, the ROIs we selected were mainly from the body of corpus callosum. The estimated neurite density fraction varied across ROIs. According to a histological post-mortem study (Aboitiz et al., 1992), fibers with a diameter below 1 μm densely populated the anterior and posterior parts of the corpus callosum with less density in the callosal midbody. Complementarily, the density of thick fibers (diameter above 3 μm) was low in the genu and splenium but showed a peak in the midbody. This was consistent with the results obtained by the histological approach from BIEL stained slices as shown in Figure 6b, the axon of the anterior part (purple-framed block) is much thinner than the body part (gray-framed block) of corpus callosum.

A significant positive correlation was found between NDI-Histology and pdFA$_{48}$ (c.c. = 0.869, p = .025), which is similar to in-vivo data. It suggests that FA's b-value dependence is connected to intra-neurite volume fraction, implying that the difference between intra- and extra-neurite diffusivity may be the cause of FA change. The post-mortem investigation with histological data provides independent evidence of neurite density. These findings support the hypothesis that FA dependence on b-value could be determined by INVF and was driven by diffusivity differences among tissue compartments.

4.3 | Model simulation results under in-vivo conditions

4.3.1 | Effect of noise on FA dependence on b-values—simulation I

It is known that signal accuracy concerns the distance between the average signal to the true value, while signal precision concerns the spread of the signal (Vis et al., 2021). Both terms are influenced by the distribution that characterizes the MR signal.

In our simulations, the Rician biased offset affects signals in terms of accuracy, while the "Gaussian" like distribution (scattered around the truth value) affects signals in terms of precision. As shown in Figure 7, the presence of noise causes the estimated FA to decrease with increasing b-values for both the multi- and single-compartment models (Figure 7a,b). The lower the SNR, the greater the decrease in FA. In the case of the low b domain (b < 1000 s/mm^2), FA is insensitive to changes in SNR, which is different from previous in-vivo research that found noise can lead to overestimation of FA at b = 1000 s/mm^2 (Farrell et al., 2007; Wang et al., 2012). On the other hand, the "Gaussian" like distribution of signal introducing a scattering of FA (shaded band in Figure 7), the lower the SNR, the larger the standard deviation is.

The effect of the rectified noise-floor on the estimated FA was previously simulated (Jones & Basser, 2004), in the high b domain (b > 3000 s/mm^2), the pattern of underestimation of the anisotropy was observed. The simulation showed that the rectified noise-floor would causing an underestimation of the ADC along the principal diffusion direction, making it more similar to radial diffusivities and thus underestimating FA. However, these simulations were limited to signal arising from a single compartment. In our multicompartment model simulation, the underestimation of the anisotropy could even be observed in the low b domain (b < 1000 s/mm^2). The estimated FA values appeared smaller than expected even under the condition without noise as Figure 7a shows. The decline in FA value will be exacerbated by a low SNR. When SNR = 30, the simulation results are fairly close to the noise-free condition.

4.3.2 | Effect of compartmental difference on FA dependence on b-values—simulation I

Our simulations of in-vivo conditions are also in good agreement with in-vivo experimental studies. As shown in Figure 7a, in pure WM (f_{iso} = 0), FA decreased with increasing b-value even in the absence of noise, if distinctive diffusivities of the intra- and extra-neurite

compartment were assumed, with the ground truth of $D_{in}^{\parallel} > D_{en}^{\perp}$. These parameter settings are in agreement with several recent reports that used different approaches to address the same question regarding compartment axial diffusivities (Dhital et al., 2019; Kunz et al., 2018; Mckinnon et al., 2018). However, in the single-compartment model, the FA value was kept constant with the same apparent diffusivities of *Simulation I* without noise (Figure 7b). These findings suggested that differences in intra- and extra-neurite compartmental diffusivity may also be responsible for the FA dependence on the *b*-value.

As an extension of DTI, multicompartment models have been studied widely in recent years (Dhital et al., 2019; Gong et al., 2020; Skinner et al., 2017; Yi et al., 2019; Zhang et al., 2012). Multicompartment diffusion models represent the total DWI signal as a sum of the diffusion-weighted signal arising from a combination of distinctive compartments with different underlying cellular microstructures, each with its own diffusivity profile. We hypothesized that the contributions of different compartments to signal generation were likely to alter when diffusion weighting changes, thus raising the FA variation derived from different *b*-shells. With increasing *b*-values, the estimated FAs decrease. This suggested that when the *b*-value is small, the intra-neurite compartment contributes more to the observed diffusion signal, due to the larger diffusivity of the intra-neurite compartment than the extra-neurite compartment, whereas when the *b*-value is large, the intra-neurite compartment contributes less. Specifically, the axial diffusivity approaches the lower extra-neurite value and the radial diffusivity approaches the intra-neurite value with the increase of the *b*-value. Whereas axial diffusivity decreases more, the observed FA would be expected smaller at a larger *b*-value. Therefore, changing the contribution of different components to the total diffusion signal by varying compartmental fractions (*INVF*) would influence pdFA. The pdFA would be higher if the actual intra-neurite fraction was higher. In general, increasing diffusion weighting will lead FA to resemble that of a compartment with lower diffusion coefficients.

4.3.3 | Interaction of compartmental difference and noise on FA dependence on *b*-value—simulation III

Due to differences in diffusion profiles, the impact of noise on intra- and extra-neurite compartment is also different. Figure 7c,d shows that the former is more sensitive to the SNR changes. In the presence of noise, the estimated FA of intra-neurite compartment decreased with the increasing *b*-values, and lower SNR made the drop larger. However, the estimated FA of the extra-neurite compartment had only a slight dependence on *b*-value. This could be due to the larger axial diffusivity of intra-compartment. As diffusion weighting increases, the signal decays more, which would be more affected by noise-floor effects. While the settled FA of the extra-compartment is very small (≈0.1), leading to similar signal attenuation degree in axial and radial directions. Hence, they are also approximately affected by the noise-floor effect, making the change of estimated FA smaller according to different diffusion weighting, which refers to *b*-value in this study. Therefore, the existence of noise amplifies the FA

dependence on the *b*-value caused by the diffusivity profile difference between compartments as we discussed in Section 4.3.2. Results of in-vivo data sets (Figure 5) and *Simulation III* (Figure 9) also supported this inference.

It is worth noting that the SNR level would have a nonlinear impact on the correlation between pdFA and NDI. For the in-vivo experiment (Figure 5), lower SNR data sets had a less significant correlation, with a larger absolute value of pdFA. Further simulations provided a more comprehensive picture with SNR levels varying from 15 to 100 and as well as noise-free conditions (Figure 9). The results identified a nonlinear effect with a trend of first increasing and then decreasing for the correlation coefficient against SNR (Figure 9b). This could be due to the loss of the specific impact of noise-floor effects on compartments as we discussed in Section 4.3.1. The *Simulation III* suggested that compartmental difference of diffusivity and noise-floor effect jointly caused the significant correlation between pdFA and *INVF*. The highest correlation coefficient can be obtained when the SNR is between 20 and 60, the presence of noise made the correlation between pdFA and NDI more significant when the SNR is lower than 60 (Figure 9b). Unlike previous studies suggested that such SNR-related variation can be substantially reduced when the SNR in raw DWIs is higher than 20 (Bastin et al., 1998; Hui et al., 2010). Hence, we concluded that diffusivity differences between intra- and extra-neurite compartments of white matter provide the basis of the observed FA dependence on *b*-values, whereas the noise-floor effects would significantly amplify this effect.

When we further studied the estimated diffusion profiles in the absence of noise (Figure 10), we discovered that diffusivity along axial direction decreased with increasing *b*-value, while radial diffusivity remained almost the same, therefore leading to an underestimation of anisotropy. The increase in INVF could make the decrease in axial diffusivity more noticeable. This indicates that as the *b*-value increases, the extra-neurite compartment with lower axial diffusivity is given more weight in the signal information. The larger the INVF, the more AD decreases, resulting in more FA changes as the *b*-value increases.

4.4 | Limitations

There are several limitations to this work. First, it is difficult to accurately match post-mortem MRI (slice thickness of 1.8 mm in this study) with histology stained slices (thickness of 6 μm) for post-mortem human brain research, which is a common challenge for most neuroimaging studies of this type (Kelm et al., 2016; Zhou et al., 2020). Due to a lack of a robust way to register the hemisphere image to an atlas, the selected ROIs on this sample were drawn manually with a certain level of subjective bias. In order to minimize this confounding factor, we used cortical anatomical landmarks to improve registration as in previous publications (Cardenas et al., 2017; Jonkman et al., 2016; Zhou et al., 2020). In future studies, research into 3D histology data (Morawski et al., 2018) is likely to become more prevalent, allowing for easier registration of MRI and histological data.

We performed a very limited set of simulations without considering the impacts of axon distribution, axonal dispersion, axon diameter, axonal undulation, and water exchange. These variables could all lead to variability in the diffusion-weighted signal generation. In addition, the difference in T2 between the intra- and extra-neurite compartments (Peled et al., 1999; Wachowicz & Snyder, 2002) may also have influence on the signal contributions between the two components. It is worth noting that NODDI derived NDI is a T_2 weighted metric (Gong et al., 2020; Veraart et al., 2019). We did not take different T_2 values of intra- and extra-neurite compartment into account, which might have some influence on the results. These factors should be considered in future work for more reliable validation.

5 | CONCLUSION

In this study, we investigated the *b*-value dependence of a range of dMRI-derived properties in the human brain, including direct comparison between post-mortem dMRI and histology. Both in-vivo and post-mortem results showed consistent declines in FA with larger *b*-values. In both experimental and simulated data, the difference in FA between high and low *b*-values is considered to be driven by noise-floor effects, the differing diffusion coefficients of intra- and extra-neurite compartments in tissue, and their interaction. These findings suggest that the microstructure of axons may be responsible for FA's *b*-value dependence in WM, and that is further amplified by the noise-floor.

AUTHOR CONTRIBUTIONS

Junye Yao: Conceptualization, resources, software, formal analysis, investigation, writing—original draft, writing—review & editing, visualization. **Benjamin C. Tendler**: Investigation, writing—review & editing. **Zihan Zhou**: Resources, investigation. **Hao Lei**: Conceptualization, writing—review & editing. **Lei Zhang**: Resources, investigation. **Aimin Bao**: Writing—review & editing, supervision, funding acquisition. **Jianhui Zhong**: Writing—review & editing, supervision. **Karla L. Miller**: Investigation, writing—review & editing, supervision. **Hongjian He**: Conceptualization, writing—review & editing, supervision, project administration, funding acquisition.

CONFLICT OF INTEREST
The authors declare no potential conflict of interest.

DATA AVAILABILITY STATEMENT
All data, models, or code generated or used during the study (including the diffusion MR images of in-vivo and post-mortem human brains, and simulation codes), are available from the corresponding author by request.

ORCID
Junye Yao https://orcid.org/0000-0002-8633-8744
Benjamin C. Tendler https://orcid.org/0000-0003-2095-8665
Hongjian He https://orcid.org/0000-0001-6272-0810

REFERENCES
Aboitiz, F., Scheibel, A. B., Fisher, R. S., & Zaidel, E. (1992). Fiber composition of the human corpus callosum. *Brain Research*, *598*, 143–153. https://doi.org/10.1016/0006-8993(92)90178-C

Alexander, D. C., Hubbard, P. L., Hall, M. G., Moore, E. A., Ptito, M., Parker, G. J. M., & Dyrby, T. B. (2010). Orientationally invariant indices of axon diameter and density from diffusion MRI. *NeuroImage*, *52*, 1374–1389. https://doi.org/10.1016/j.neuroimage.2010.05.043

Aliotta, E., Nourzadeh, H., Sanders, J., Muller, D., & Ennis, D. B. (2019). Highly accelerated, model-free diffusion tensor MRI reconstruction using neural networks. *Medical Physics*, *46*, 1581–1591. https://doi.org/10.1002/mp.13400

Asken, B. M., Dekosky, S. T., Clugston, J. R., Jaffee, M. S., & Bauer, R. M. (2018). Diffusion tensor imaging (DTI) findings in adult civilian, military, and sport-related mild traumatic brain injury (mTBI): A systematic critical review. *Brain Imaging and Behavior*, *12*, 585–612. https://doi.org/10.1007/s11682-017-9708-9

Bagnato, F., Hametner, S., Boyd, E., Endmayr, V., Shi, Y., Ikonomidou, V., Chen, G., Pawate, S., Lassmann, H., Smith, S., & Welch, E. B. (2018). Untangling the R2* contrast in multiple sclerosis: A combined MRI-histology study at 7.0 Tesla. *PLoS One*, *13*, e0193839. https://doi.org/10.1371/journal.pone.0193839

Barrio-Arranz, G., De Luis-García, R., Tristán-Vega, A., Martín-Fernández, M., & Aja-Fernández, S. (2015). Impact of MR acquisition parameters on DTI scalar indexes: A tractography based approach. *PLoS One*, *10*, e0137905. https://doi.org/10.1371/journal.pone.0137905

Basser, P. J. (1995). Inferring microstructural features and the physiological state of tissues from diffusion-weighted images. *NMR in Biomedicine*, *8*, 333–344. https://doi.org/10.1002/nbm.1940080707

Bastin, M. E., Armitage, P. A., & Marshall, I. (1998). A theoretical study of the effect of experimental noise on the measurement of anisotropy in diffusion imaging. *Magnetic Resonance Imaging*, *16*, 773–785. https://doi.org/10.1016/S0730-725X(98)00098-8

Benjamini, Y., & Hochberg, Y. (1995). Controlling the false discovery rate: A practical and powerful approach to multiple testing. *Journal of the Royal Statistical Society*, *Series B*, *57*, 289–300. https://doi.org/10.1111/j.2517-6161.1995.tb02031.x

Clark, C. A., & Bihan, D. L. (2000). Water diffusion compartmentation and anisotropy at high *b* values in the human brain. *Magnetic Resonance in Medicine*, *44*, 852–859. https://doi.org/10.1002/1522-2594

Bihan, D. L. (2007). The 'wet mind': Water and functional neuroimaging. *Physics in Medicine and Biology*, *52*, 57–90. https://doi.org/10.1088/0031-9155/52

Bisdas, S., Bohning, D. E., Besenski, N., Nicholas, J. S., & Rumboldt, Z. (2008). Reproducibility, interrater agreement, and age-related changes of fractional anisotropy measures at 3T in healthy subjects: Effect of the applied *b*-value. *AJNR. American Journal of Neuroradiology*, *29*, 1128–1133. https://doi.org/10.3174/ajnr.A1044

Bledsoe, I. O., Stebbins, G. T., Merkitch, D., & Goldman, J. G. (2018). White matter abnormalities in the corpus callosum with cognitive impairment in Parkinson disease. *Neurology*, *91*, e2244–e2255. https://doi.org/10.1212/wnl.0000000000006646

Cardenas, A. M., Sarlls, J. E., Kwan, J. Y., Bageac, D., Gala, Z. S., Danielian, L. E., Ray-Chaudhury, A., Wang, H.-W., Miller, K. L.,

Foxley, S., Jbabdi, S., Welsh, R. C., & Floeter, M. K. (2017). Pathology of callosal damage in ALS: An ex-vivo, 7 T diffusion tensor MRI study. *NeuroImage: Clinical*, *15*, 200–208. https://doi.org/10.1016/j.nicl.2017.04.024

Chang, Y. S., Owen, J. P., Pojman, N. J., Thieu, T., Bukshpun, P., Wakahiro, M. L. J., Berman, J. I., Roberts, T. P. L., Nagarajan, S. S., Sherr, E. H., & Mukherjee, P. (2015). White matter changes of neurite density and fiber orientation dispersion during human brain maturation. *PLoS One*, *10*, e0123656. https://doi.org/10.1371/journal.pone.0123656

Clark, C. A., Hedehus, M., & Moseley, M. E. (2002). In vivo mapping of the fast and slow diffusion tensors in human brain. *Magnetic Resonance in Medicine*, *47*, 623–628. https://doi.org/10.1002/mrm.10118

Coelho, S., Pozo, J. M., Costantini, M., Highley, J. R., Mozumder, M., Simpson, J. E., Ince, P. G., & Frangi, A. F. (2018). Local volume fraction distributions of axons, astrocytes, and myelin in deep subcortical white matter. *NeuroImage*, *179*, 275–287. https://doi.org/10.1016/j.neuroimage.2018.06.040

D'Arceuil, H. E., Westmoreland, S., & de Crespigny, A. J. (2007). An approach to high resolution diffusion tensor imaging in fixed primate brain. *NeuroImage*, *35*, 553–565. https://doi.org/10.1016/j.neuroimage.2006.12.028

den Dekker, A. J., & Sijbers, J. (2014). Data distributions in magnetic resonance images: A review. *Physica Medica*, *30*, 725–741. https://doi.org/10.1016/j.ejmp.2014.05.002

Dhital, B., Kellner, E., Kiselev, V. G., & Reisert, M. (2018). The absence of restricted water pool in brain white matter. *NeuroImage*, *182*, 398–406. https://doi.org/10.1016/j.neuroimage.2017.10.051

Dhital, B., Reisert, M., Kellner, E., & Kiselev, V. G. (2019). Intra-axonal diffusivity in brain white matter. *NeuroImage*, *189*, 543–550. https://doi.org/10.1016/j.neuroimage.2019.01.015

Farrell, J. A. D., Landman, B. A., Jones, C. K., Smith, S. A., Prince, J. L., Van Zijl, P. C. M., & Mori, S. (2007). Effects of signal-to-noise ratio on the accuracy and reproducibility of diffusion tensor imaging-derived fractional anisotropy, mean diffusivity, and principal eigenvector measurements at 1.5T. *Journal of Magnetic Resonance Imaging*, *26*, 756–767. https://doi.org/10.1002/jmri.21053

Fukutomi, H., Glasser, M. F., Murata, K., Akasaka, T., Fujimoto, K., Yamamoto, T., Autio, J. A., Okada, T., Togashi, K., Zhang, H., Van Essen, D. C., & Hayashi, T. (2019). Diffusion tensor model links to neurite orientation dispersion and density imaging at high *b*-value in cerebral cortical gray matter. *Scientific Reports*, *9*, 12246. https://doi.org/10.1038/s41598-019-48671-7

Fukutomi, H., Glasser, M. F., Zhang, H., Autio, J. A., Coalson, T. S., Okada, T., Togashi, K., Essen, D. C. V., & Hayashi, T. (2018). Neuro-Image neurite imaging reveals microstructural variations in human cerebral cortical gray matter. *NeuroImage*, *182*, 488–499. https://doi.org/10.1016/j.neuroimage.2018.02.017

Glasser, M. F., Coalson, T. S., Robinson, E. C., Hacker, C. D., Harwell, J., Yacoub, E., Ugurbil, K., Andersson, J., Beckmann, C. F., Jenkinson, M., Smith, S. M., & Van Essen, D. C. (2016). A multi-modal parcellation of human cerebral cortex. *Nature*, *536*, 171–178. https://doi.org/10.1038/nature18933

Gong, T., Tong, Q., He, H., Sun, Y., Zhong, J., & Zhang, H. (2020). MTE-NODDI: Multi-TE NODDI for disentangling non-T2-weighted signal fractions from compartment-specific T2 relaxation times. *NeuroImage*, *217*, 116906. https://doi.org/10.1016/j.neuroimage.2020.116906

Gudbjartsson, H., & Patz, S. (1995). The rician distribution of noisy MRI data. *Magnetic Resonance in Medicine*, *34*, 910–914. https://doi.org/10.1002/mrm.1910340618

Guo, G., Zhu, L.-H., Zhang, Z.-P., Wang, F.-N., & Cheng, Q.-H. (2019). Diffusion kurtosis imaging of microstructural changes in brain tissue affected by acute ischemic stroke in different locations. *Neural Regeneration Research*, *14*, 272–279. https://doi.org/10.4103/1673-5374.244791

Harms, R. L., Fritz, F. J., Tobisch, A., Goebel, R., & Roebroeck, A. (2017). Robust and fast nonlinear optimization of diffusion MRI microstructure models. *NeuroImage*, *155*, 82–96. https://doi.org/10.1016/j.neuroimage.2017.04.064

Hofer, S., & Frahm, J. (2006). Topography of the human corpus callosum revisited—Comprehensive fiber tractography using diffusion tensor magnetic resonance imaging. *NeuroImage*, *32*, 989–994. https://doi.org/10.1016/j.neuroimage.2006.05.044

Hui, E. S., Cheung, M. M., Chan, K. C., & Wu, E. X. (2010). *B*-value dependence of DTI quantitation and sensitivity in detecting neural tissue changes. *NeuroImage*, *49*, 2366–2374. https://doi.org/10.1016/j.neuroimage.2009.10.022

Hui, E. S., Cheung, M. M., Qi, L., & Wu, E. X. (2008). Towards better MR characterization of neural tissues using directional diffusion kurtosis analysis. *NeuroImage*, *42*, 122–134. https://doi.org/10.1016/j.neuroimage.2008.04.237

Jensen, J. H., Helpern, J. A., Ramani, A., Lu, H., & Kaczynski, K. (2005). Diffusional kurtosis imaging: The quantification of non-gaussian water diffusion by means of magnetic resonance imaging. *Magnetic Resonance in Medicine*, *53*, 1432–1440. https://doi.org/10.1002/mrm.20508

Jespersen, S. N., Olesen, J. L., Hansen, B., & Shemesh, N. (2018). Diffusion time dependence of microstructural parameters in fixed spinal cord. *NeuroImage*, *182*, 329–342. https://doi.org/10.1016/j.neuroimage.2017.08.039

Jones, D. K., & Basser, P. J. (2004). "Squashing peanuts and smashing pumpkins": How noise distorts diffusion-weighted MR data. *Magnetic Resonance in Medicine*, *52*, 979–993. https://doi.org/10.1002/mrm.20283

Jonkman, L. E., Graaf, Y. G. D., Bulk, M., Kaaij, E., Pouwels, P. J. W., Barkhof, F., Rozemuller, A. J. M., van der Weerd, L., Geurts, J. J. G., & van de Berg, W. D. J. (2019). Normal aging brain collection Amsterdam (NABCA): A comprehensive collection of postmortem high-field imaging, neuropathological and morphometric datasets of non-neurological controls. *NeuroImage: Clinical*, *22*, 101698. https://doi.org/10.1016/j.nicl.2019.101698

Jonkman, L. E., Klaver, R., Fleysher, L., Inglese, M., & Geurts, J. J. G. (2016). The substrate of increased cortical FA in MS: A 7T post-mortem MRI and histopathology study. *Multiple Sclerosis Journal*, *22*, 1804–1811. https://doi.org/10.1177/1352458516635290

Kamiya, K., Hori, M., & Aoki, S. (2020). NODDI in clinical research. *Journal of Neuroscience Methods*, *346*, 108908. https://doi.org/10.1016/j.jneumeth.2020.108908

Kantarci, K., Murray, M. E., Schwarz, C. G., Reid, R. I., Przybelski, S. A., Lesnick, T., Zuk, S. M., Raman, M. R., Senjem, M. L., Gunter, J. L., Boeve, B. F., Knopman, D. S., Parisi, J. E., Petersen, R. C., Jack, C. R., & Dickson, D. W. (2017). White-matter integrity on DTI and the pathologic staging of Alzheimer's disease. *Neurobiology of Aging*, *56*, 172–179. https://doi.org/10.1016/j.neurobiolaging.2017.04.024

Kelm, N. D., West, K. L., Carson, R. P., Gochberg, D. F., Ess, K. C., & Does, M. D. (2016). Evaluation of diffusion kurtosis imaging in ex vivo hypomyelinated mouse brains. *NeuroImage*, *124*, 612–626. https://doi.org/10.1016/j.neuroimage.2015.09.028

Kunz, N., Da Silva, A. R., & Jelescu, I. O. (2018). Intra- and extra-axonal axial diffusivities in the white matter: Which one is faster? *NeuroImage*, *181*, 314–322. https://doi.org/10.1016/j.neuroimage.2018.07.020

Landman, B. A., Farrell, J. A. D., Jones, C. K., Smith, S. A., Prince, J. L., & Mori, S. (2007). Effects of diffusion weighting schemes on the reproducibility of DTI-derived fractional anisotropy, mean diffusivity, and principal eigenvector measurements at 1.5T. *NeuroImage*, *36*, 1123–1138. https://doi.org/10.1016/j.neuroimage.2007.02.056

Lerma-Usabiaga, G., Mukherjee, P., Ren, Z., Perry, M. L., & Wandell, B. A. (2019). Replication and generalization in applied neuroimaging. *NeuroImage*, *202*, 116048. https://doi.org/10.1016/j.neuroimage.2019.116048

Lu, H., Jensen, J. H., Ramani, A., & Helpern, J. A. (2006). Three-dimensional characterization of non-gaussian water diffusion in humans using diffusion kurtosis imaging. *NMR in Biomedicine*, *19*, 236–247. https://doi.org/10.1002/nbm.1020

Maj, E., Szemplińska, B., Szeszkowski, W., Prokopienko, M., Cieszanowski, A., Marchel, A., & Rowiński, O. (2020). Role of diffusion tensor imaging parameters in the characterization and differentiation of infiltrating and non-infiltrating spinal cord tumors. *Clinical Neuroradiology*, *30*, 739–747. https://doi.org/10.1007/s00062-019-00851-8

Marques, J. P., Kober, T., Krueger, G., van der Zwaag, W., Van de Moortele, P. F., & Gruetter, R. (2010). MP2RAGE, a self bias-field corrected sequence for improved segmentation and T1-mapping at high field. *NeuroImage*, *49*, 1271–1281. https://doi.org/10.1016/j.neuroimage.2009.10.002

Mårtensson, J., Lätt, J., Åhs, F., Fredrikson, M., Söderlund, H., Schiöth, H. B., Kok, J., Kremer, B., Van Westen, D., Larsson, E.-M., & Nilsson, M. (2018). Diffusion tensor imaging and tractography of the white matter in normal aging: The rate-of-change differs between segments within tracts. *Magnetic Resonance Imaging*, *45*, 113–119. https://doi.org/10.1016/j.mri.2017.03.007

Mckinnon, E. T., Helpern, J. A., & Jensen, J. H. (2018). Modeling white matter microstructure with fiber ball imaging. *NeuroImage*, *176*, 11–21. https://doi.org/10.1016/j.neuroimage.2018.04.025

Melhem, E. R., Itoh, R., Jones, L., & Barker, P. B. (2000). Diffusion tensor MR imaging of the brain: Effect of diffusion weighting on trace and anisotropy measurements. *American Journal of Neuroradiology*, *21*, 1813–1820.

Metzler-Baddeley, C., O'Sullivan, M. J., Bells, S., Pasternak, O., & Jones, D. K. (2012). How and how not to correct for CSF-contamination in diffusion MRI. *NeuroImage*, *59*, 1394–1403. https://doi.org/10.1016/j.neuroimage.2011.08.043

Morawski, M., Kirilina, E., Scherf, N., Jäger, C., Reimann, K., Trampel, R., Gavriilidis, F., Geyer, S., Biedermann, B., Arendt, T., & Weiskopf, N. (2018). Developing 3D microscopy with CLARITY on human brain tissue: Towards a tool for informing and validating MRI-based histology. *NeuroImage*, *182*, 417–428. https://doi.org/10.1016/j.neuroimage.2017.11.060

Mori, S., & Zhang, J. (2006). Principles of diffusion tensor imaging and its applications to basic neuroscience research. *Neuron*, *51*, 527–539. https://doi.org/10.1016/j.neuron.2006.08.012

Mori, S., Wakana, S., van Zijl, P. C. M., & Nagae-Poetscher, L. M. (2005). *MRI Atlas of Human White Matter*. Elsevier, Amsterdam, The Netherlands.

Mukherjee, P., Chung, S. W., Berman, J. I., Hess, C. P., & Henry, R. G. (2008). Diffusion tensor MR imaging and fiber tractography: Technical considerations. *American Journal of Neuroradiology*, *29*, 843–852. https://doi.org/10.3174/ajnr.a1052

Niendorf, T., Dijkhuizen, R. M., Norris, D. G., Van Lookeren Campagne, M., & Nicolay, K. (1996). Biexponential diffusion attenuation in various states of brain tissue: Implications for diffusion-weighted imaging. *Magnetic Resonance in Medicine*, *36*, 847–857. https://doi.org/10.1002/mrm.1910360607

Novikov, D. S., Fieremans, E., Jespersen, S. N., & Kiselev, V. G. (2019). Quantifying brain microstructure with diffusion MRI: Theory and parameter estimation. *NMR in Biomedicine*, *32*, e3998. https://doi.org/10.1002/nbm.3998

Olvet, D. M., Peruzzo, D., Thapa-Chhetry, B., Sublette, M. E., Sullivan, G. M., Oquendo, M. A., Mann, J. J., & Parsey, R. V. (2014). A diffusion tensor imaging study of suicide attempters. *Journal of Psychiatric Research*, *51*, 60–67. https://doi.org/10.1016/j.jpsychires.2014.01.002

Peled, S., Cory, D. G., Raymond, S. A., Kirschner, D. A., & Jolesz, F. A. (1999). Water diffusion, T2, and compartmentation in frog sciatic nerve. *Magnetic Resonance in Medicine*, *42*, 911–918. https://doi.org/10.1002/(SICI)1522-2594(199911)42:5<911::AID-MRM11>3.0.CO;2-J

Pierpaoli, C., & Basser, P. J. (1996). Toward a quantitative assessment of diffusion anisotropy. *Magnetic Resonance in Medicine*, *36*, 893–906. https://doi.org/10.1002/mrm.1910360612

Porter, D. A., & Heidemann, R. M. (2009). High resolution diffusion-weighted imaging using readout-segmented echo-planar imaging, parallel imaging and a two-dimensional navigator-based reacquisition. *Magnetic Resonance in Medicine*, *62*, 468–475. https://doi.org/10.1002/mrm.22024

Qiu, A., Mori, S., & Miller, M. I. (2015). Diffusion tensor imaging for understanding brain development in early life. *Annual Review of Psychology*, *66*, 853–876. https://doi.org/10.1146/annurev-psych-010814-015340

Raab, P., Hattingen, E., Franz, K., Zanella, F. E., & Lanfermann, H. (2010). Cerebral gliomas: Diffusional kurtosis imaging analysis of microstructural differences. *Radiology*, *254*, 876–881. https://doi.org/10.1148/radiol.09090819

Repple, J., Meinert, S., Grotegerd, D., Kugel, H., Redlich, R., Dohm, K., Zaremba, D., Opel, N., Buerger, C., Förster, K., Nick, T., Arolt, V., Heindel, W., Deppe, M., & Dannlowski, U. (2017). A voxel-based diffusion tensor imaging study in unipolar and bipolar depression. *Bipolar Disorders*, *19*, 23–31. https://doi.org/10.1111/bdi.12465

Schmierer, K., Scaravilli, F., Altmann, D. R., Barker, G. J., & Miller, D. H. (2004). Magnetization transfer ratio and myelin in postmortem multiple sclerosis brain. *Annals of Neurology*, *56*, 407–415. https://doi.org/10.1002/ana.20202

Setsompop, K., Gagoski, B. A., Polimeni, J. R., Witzel, T., Wedeen, V. J., & Wald, L. L. (2012). Blipped-controlled aliasing in parallel imaging for simultaneous multislice echo planar imaging with reduced g -factor penalty. *Magnetic Resonance in Medicine*, *67*, 1210–1224. https://doi.org/10.1002/mrm.23097

Shepherd, T. M., Thelwall, P. E., Stanisz, G. J., & Blackband, S. J. (2009). Aldehyde fixative solutions alter the water relaxation and diffusion properties of nervous tissue. *Magnetic Resonance in Medicine*, *62*, 26–34. https://doi.org/10.1002/mrm.21977

Skinner, N. P., Kurpad, S. N., Schmit, B. D., Tugan Muftuler, L., & Budde, M. D. (2017). Rapid in vivo detection of rat spinal cord injury with double-diffusion-encoded magnetic resonance spectroscopy. *Magnetic Resonance in Medicine*, *77*, 1639–1649. https://doi.org/10.1002/mrm.26243

Stejskal, E. O., & Tanner, J. E. (1965). Spin diffusion measurements: Spin echoes in the presence of a time-dependent field gradient. *The Journal of Chemical Physics*, *42*, 288–292. https://doi.org/10.1063/1.1695690

Tuch, D. S. (2004). Q-ball imaging. *Magnetic Resonance in Medicine*, *52*, 1358–1372. https://doi.org/10.1002/mrm.20279

Van Essen, D. C., Smith, S. M., Barch, D. M., Behrens, T. E. J., Yacoub, E., & Ugurbil, K. (2013). The WU-Minn human connectome project: An overview. *NeuroImage*, *80*, 62–79. https://doi.org/10.1016/j.neuroimage.2013.05.041

Veraart, J., Fieremans, E., & Novikov, D. S. (2019). On the scaling behavior of water diffusion in human brain white matter. *NeuroImage*, *185*, 379–387. https://doi.org/10.1016/j.neuroimage.2018.09.075

Veraart, J., Poot, D. H. J., Hecke, W. V., Blockx, I., Linden, A. V. D., Verhoye, M., & Sijbers, J. (2011). More accurate estimation of diffusion tensor parameters using diffusion kurtosis imaging. *Magnetic Resonance in Medicine*, *65*, 138–145. https://doi.org/10.1002/mrm.22603

Vis, G., Nilsson, M., Westin, C. F., & Szczepankiewicz, F. (2021). Accuracy and precision in super-resolution MRI: Enabling spherical tensor diffusion encoding at ultra-high b-values and high resolution. *NeuroImage*, *245*, 118673. https://doi.org/10.1016/j.neuroimage.2021.118673

Wachowicz, K., & Snyder, R. E. (2002). Assignment of the T2 components of amphibian peripheral nerve to their microanatomical compartments. *Magnetic Resonance in Medicine*, *47*, 239–245. https://doi.org/10.1002/mrm.10053

Wang, J. Y., Abdi, H., Bakhadirov, K., Diaz-Arrastia, R., & Devous, M. D. (2012). A comprehensive reliability assessment of quantitative

diffusion tensor tractography. *NeuroImage*, *60*, 1127–1138. https://doi.org/10.1016/j.neuroimage.2011.12.062

Wu, Y., Zou, C., Liu, W., Liao, W., Yang, W., Porter, D. A., Liu, X., & Wu, E. X. (2013). Effect of *B*-value in revealing postinfarct myocardial microstructural remodeling using MR diffusion tensor imaging. *Magnetic Resonance Imaging*, *31*, 847–856. https://doi.org/10.1016/j.mri.2013.02.010

Yi, S. Y., Barnett, B. R., Torres-Velázquez, M., Zhang, Y., Hurley, S. A., Rowley, P. A., Hernando, D., & Yu, J. P. J. (2019). Detecting microglial density with quantitative multi-compartment diffusion MRI. *Frontiers in Neuroscience*, *13*, 1–9. https://doi.org/10.3389/fnins.2019.00081

Zhang, H., Hubbard, P. L., Parker, G. J. M., & Alexander, D. C. (2011). Axon diameter mapping in the presence of orientation dispersion with diffusion MRI. *NeuroImage*, *56*, 1301–1315. https://doi.org/10.1016/j.neuroimage.2011.01.084

Zhang, H., Schneider, T., Wheeler-Kingshott, C. A., & Alexander, D. C. (2012). NODDI: Practical in vivo neurite orientation dispersion and density imaging of the human brain. *NeuroImage*, *61*, 1000–1016. https://doi.org/10.1016/j.neuroimage.2012.03.072

Zhou, Z., Tong, Q., Zhang, L., Ding, Q., Lu, H., Jonkman, L. E., Yao, J., He, H., Zhu, K., & Zhong, J. (2020). Evaluation of the diffusion MRI white matter tract integrity model using myelin histology and Monte-Carlo simulations. *NeuroImage*, *223*, 117313. https://doi.org/10.1016/j.neuroimage.2020.117313

SUPPORTING INFORMATION

Additional supporting information can be found online in the Supporting Information section at the end of this article.